A Metric for Finding Robust Start Positions for Medical Steerable Needle Automation

Janine Hoelscher[1], Inbar Fried[1], Mengyu Fu[1], Mihir Patwardhan[1], Max Christman[1],
Jason Akulian[2], Robert J. Webster III[3], Ron Alterovitz[1]

***Abstract*— Steerable needles are medical devices with the ability to follow curvilinear paths to reach targets while circumventing obstacles. In the deployment process, a human operator typically places the steerable needle at its start position on a tissue surface and then hands off control to the automation that steers the needle to the target. Due to uncertainty in the placement of the needle by the human operator, choosing a start position that is robust to deviations is crucial since some start positions may make it impossible for the steerable needle to safely reach the target. We introduce a method to efficiently evaluate steerable needle motion plans such that they are safe to variation in the start position. This method can be applied to many steerable needle planners and requires that the needle's orientation angle at insertion can be robotically controlled. Specifically, we introduce a method that builds a funnel around a given plan to determine a safe insertion surface corresponding to insertion points from which it is guaranteed that a collision-free motion plan to the goal can be computed. We use this technique to evaluate multiple feasible plans and select the one that maximizes the size of the safe insertion surface. We evaluate our method through simulation in a lung biopsy scenario and show that the method is able to quickly find needle plans with a large safe insertion surface.**

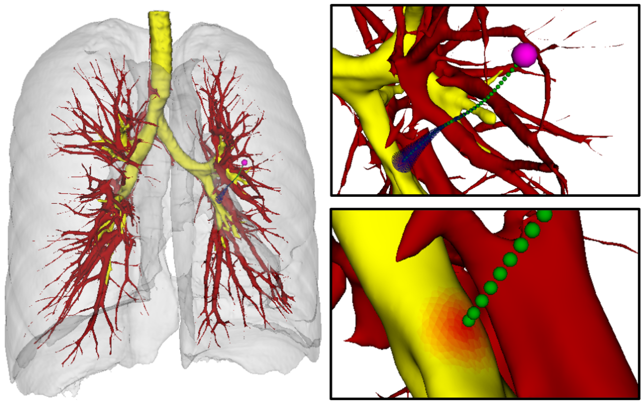

Fig. 1. We demonstrate our method in a lung biopsy scenario where a steerable needle is inserted from the airways (yellow) into the lung parenchyma (grey) and is steered towards a target (pink) while avoiding large blood vessels (dark red). Our method constructs a funnel (blue) along a steerable needle motion plan (green) such that the target can be reached from any position inside the funnel. Our method computes a valid insertion surface (orange and red) for which collision-free plans to the target can be found. Darker coloring corresponds to a larger distance to the surface boundary and therefore more robustness to deviations.

I. INTRODUCTION

Steerable needles are medical devices that allow for minimally invasive medical procedures in a variety of environments, e.g., in the lung [1], brain [2], and liver [3]. They are able to bend and follow curvilinear paths in tissue [4]. This feature enables obstacle avoidance, i.e., steerable needles can circumvent critical anatomical obstacles, and thereby mitigate patient risk. However, deploying a steerable needle along a curved obstacle-avoiding path to a physician-specified target is a complex process that is non-intuitive to humans [5]. Therefore, a variety of motion planning algorithms and control strategies have been developed to automate the needle steering.

In a typical steerable needle deployment scenario, a motion planner determines a collision-free motion plan for the steerable needle, including a start position. The human operator aims to place the steerable needle at this start position for which a path to the target is known to be possible. The start position is typically located on an insertion surface such as the skin or other tissue surface. Once the human operator has placed the needle at its start position, the human hands off control to the automation, and the steerable needle can begin autonomously steering through tissue to the target. Accuracy during this hand-off from the human to the automation is critical for the success of the overall procedure. Even a small deviation from the planned start position requires recomputing the entire motion plan to the target, and there is no guarantee that the target can still be reached due to obstacles and kinematic constraints. Quantifying a level of robustness to deviations in the hand-off position is important to account for inevitable deviations due to operator errors or preferences.

In this work, we introduce a new metric for steerable needle motion planning that evaluates plans based on their robustness with respect to deviations in their start positions. Since there is often uncertainty in the initial placement of the steerable needle due to human or mechanical imprecision, selecting a position that is robust to errors has the potential to improve the likelihood that the procedure can be successfully performed. Our new metric aims to convey to the (human)

This research was supported by the U.S. National Institutes of Health (NIH) under award R01EB024864 and the National Science Foundation (NSF) under awards 2008475 and 2038855.

[1] J. Hoelscher, I. Fried, M. Fu, M. Patwardhan, M. Christman, and R. Alterovitz are with the Department of Computer Science, University of North Carolina at Chapel Hill, Chapel Hill, NC 27599, USA. {jhoelsch, ifried01, mfu, ron}@cs.unc.edu, {mihir01, mrlc}@live.unc.edu

[2] J. A. Akulian is with the Division of Pulmonary Diseases and Critical Care Medicine at the University of North Carolina at Chapel Hill, NC 27599, USA. jason_akulian@med.unc.edu

[3] R. J. Webster III is with the Department of Mechanical Engineering, Vanderbilt University, Nashville, TN 37235, USA. robert.webster@vanderbilt.edu

operator a valid insertion surface from which the target can be reached and how much deviation in the hand-off position the automated system can compensate for, as shown in Fig. 1.

We also describe an efficient strategy to compute the introduced metric by determining a valid insertion surface based on a nominal motion plan. This strategy can be used in combination with many existing steerable needle motion planners. Furthermore, we describe a method to efficiently plan nominal motion plans from a surface region to a target point using existing needle planners.

The valid insertion surface is limited by the steerable needle's hardware constraints and is further limited by the presence of obstacles. We determine this surface by constructing a funnel along the plan that we project onto the insertion surface. The funnel starts as a point at the target and grows in diameter as it approaches the insertion surface, and its diameter along the nominal motion plan is constrained such that for each position inside the funnel we can guarantee that a collision-free plan to the target exists. Our method assumes that the steerable needle can be automatically rotated at its insertion point to set the orientation of the insertion pose, which can be achieved e.g., with an aiming device as described in [6]. We then create a "bullseye" visualization of the valid insertion surface, as shown in Fig. 1, that provides visual guidance to a human operator for aiming the steerable needle towards its desired hand-off position.

Our main contributions in this paper are: (i) a new insertion robustness metric for steerable needle plans and (ii) a method to efficiently compute this metric – namely, a funnel shape constructed around a needle plan – that can be applied to many steerable needle planners.

We evaluate our method in simulation for a biopsy procedure planning scenario in a human lung. In this scenario, a physician deploys a steerable needle through the airway wall before a robot autonomously steers it to the biopsy location. To demonstrate its versatility, we apply our funnel computation method to plans computed by two different steerable needle motion planners: the steerable needle RRT [7] and an AO-RRT [8] adapted to steerable needles. We also show that our funnel method is more efficient than a previously-developed sampling-based strategy in evaluating plans according to our proposed start position robustness metric.

II. RELATED WORK

Robotic steerable needles are a promising approach to reach parts of the body not safely reachable with conventional instruments [9]. A variety of motion planners aim to find safe needle plans that pose low risk to patients. These planners employ different approaches, including search based planning [10], fractal-based planning [2], and optimization methods [11]. Sampling-based motion planning is another planning approach that has been shown to be effective in many applications with high dimensional configuration spaces. Patil et al. [12] introduced a steerable needle motion planner that creates a Rapidly-exploring Random Tree (RRT) [13] from a start pose to a goal position.

Many motion planning algorithms exist for different types or robots that plan from a specific start pose to a target region [14], [15], [16], but few works explore planning from a start region to a target position, as in most planning scenarios, at least an approximate start pose of the robot is known. Alterovitz et al. introduced a method to compute an optimal needle plan in 2D from an insertion region [17]. Kuntz et al. considered the automatic delivery of the robot to its initial pose as an additional planning stage [18]. In this paper, we use a variation of the backward planing strategy we previously introduced [19]. The backward planner creates multiple interleaving RRTs growing from the target position towards a start region by sampling new target poses with a certain probability during the planning process. This backward planning process can be applied with little adaptation to any pose-to-point steerable needle planner.

Prior work has investigated choosing a port location and initial robot pose for minimally invasive procedures optimizing the angle of the surgical tool and reachability of the target [20], [21], [22], [23]. Sun et al. introduce a method to evaluate all locations on an insertion surface based on criteria such as visibility and physician preference [24]. All these systems use minimally invasive tools that only allow for straight insertions and thus do not require motion planning to determine target reachability. Niyaz et al. consider the selection of an insertion pose of a concentric tube robot as part of the problem setup and their method interleaves optimizing the setup and motion planning to a target to find the best combination of the two [25].

Beyond medical applications, the notion of hand-offs occurs in planning scenarios as interactions between multiple agents passing objects from one agent to another. Planning strategies exist both for heterogeneous multi-agent systems [26] and systems with two robot arms (e.g., for assembly tasks) [27], [28]. These planning strategies require precise models of the reachable workspaces of all agents. In the case of hand-offs between humans and robots, this knowledge is not freely available. In [29], the planner includes a trust metric measuring the predictability of the human's behavior, and, in the case of unexpected human movement, leads the robot to move more cautiously towards a hand-off. Mainprice et al. [30] take into account human mobility and plan for the most efficient hand-off location by estimating how fast a human can reach it. Vahrenkamp et al. [31] define an interaction workspace for hand-offs between humans and robots that can be reached by both agents. However, to our knowledge, there exists no method that evaluates hand-off positions by their robustness to uncertainty.

In this work, we are not only interested in finding a plan from a position within a start region, but we are also interested in the robustness to changes in this position to account for potential error prior to needle insertion. A related concept is steerable needle motion planning considering uncertainty during robot deployment [32], [33], [34], [35]. Favaro et al. introduce a steerable catheter motion planner that plans from a fixed insertion pose and creates motion plans optimal with respect to their robustness to control error during deployment [36]. Tedrake integrates RRT motion planning and LQR-based robot control [37]. This method ensures that initial conditions able to reach the target will stabilize to the target, but it does not provide any means to determine these initial conditions.

III. PROBLEM DEFINITION

The planning scenario consists of a 3D workspace $\mathcal{W} \subset \mathbb{R}^3$. The workspace contains obstacles $\mathcal{O} \subset \mathcal{W}$ that the steerable needle should not collide with. The steerable needle's tip should reach a target position $\mathbf{p}_{\text{target}} \in \mathcal{W}$. The steerable needle can be inserted from any position on an insertion surface S embedded in $\mathcal{W}$.

We model the kinematics of the steerable needle using a 3D unicycle model [32], [38]. The steerable needle is flexible and curves in the direction of its beveled tip when it is inserted, following a constant curvature arc in a plane. The steerable needle's reachable workspace is limited by its minimum radius of curvature r_{min}. Arcs with larger radii can be achieved through duty cycling [39]. Axially twisting the steerable needle's base changes the plane of curvature and thereby the direction of steering. The planner also needs to take into account additional hardware constraints, in particular, the steerable needle's cross-sectional diameter d_{needle} and its maximum insertion length l_{needle}. We assume that the steerable needle follows its tip in a follow-the-leader manner [40]. Therefore, we can describe the configuration of the steerable needle by the pose of its tip. We denote a steerable needle configuration $\mathbf{q}_i$ as a 4×4 homogeneous transformation matrix:

$$\mathbf{q}_i = \begin{pmatrix} \mathbf{R}_i & \mathbf{p}_i \\ \mathbf{0} & 1 \end{pmatrix},$$

where $\mathbf{p}_i \in \mathbb{R}^3$ is a position relative to a world coordinate frame and $\mathbf{R}_i \in SO(3)$ is the steerable needle tip's orientation. We model the steerable needle's movement such that the steerable needle moves in direction $\mathbf{R}_i^z$ and curves into direction $-\mathbf{R}_i^y$. We assume that an aiming device rotates the steerable needle at its insertion position toward the desired orientation.

Based on the steerable needle's kinematic model, constant curvature arcs connect consecutive configurations of the needle plan. We describe arcs by a radius of curvature r, an insertion length l, and a rotation around the steerable needle's deployment direction $\gamma \in [0, 2\pi]$. We define a section of a steerable needle motion plan as $\rho_i = \{\mathbf{q}_i, r_i, l_i, \gamma_i\}$, where the constant curvature arc described by r_i, l_i, and γ_i connects $\mathbf{q}_i$ and the consecutive configuration $\mathbf{q}_{i+1}$. A steerable needle motion plan is an ordered list $\Pi = [\rho_1, \dots, \rho_n]$ of $n \in \mathbb{N}$ plan sections. Plan section ρ_n connects to the target $\mathbf{p}_{\text{target}}$. No plan section can intersect with an obstacle in $\mathcal{O}$.

We introduce a start position robustness metric $R(\Pi, S) \mapsto \mathbb{R}$ that expresses the tolerance to deviations in the start position for a nominal motion plan Π as shown in Fig. 2. We define $U \subset S$ as the valid insertion surface from which the target can be reached. Metric R is the radius w of U projected onto the plane tangent to start pose $\mathbf{q}_1$:

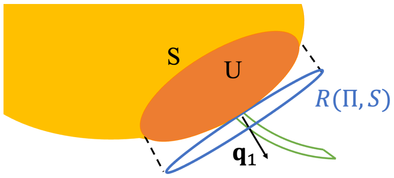

Fig. 2. Following a nominal motion plan Π, the steerable needle is inserted from surface S (yellow) at $\mathbf{q}_1$. We evaluate this start pose using robustness metric $R(\Pi, S)$. This metric is the radius of a circle on a plane tangent to the start pose. We guarantee for all positions within this circle that a plan to the target exists. We project the circle onto surface S to determine a valid insertion surface U (orange).

$$R(\Pi, S) = \max\ w \text{ s. t. } ||\mathbf{s}' - \mathbf{p}_1||_2 > w \ \forall \mathbf{s} \in S \setminus U, \quad (1)$$

where $\mathbf{s} \in \mathbb{R}^3$ represents positions on surface S not contained in valid insertion surface U, $\mathbf{s}' \in \mathbb{R}^3$ is the projection of $\mathbf{s}$ onto the plane tangent to $\mathbf{q}_1$, and $\mathbf{p}_1 \in \mathbb{R}^3$ is the start position. This metric guarantees that for any position on U, a collision-free steerable needle motion plan to the target can be found.

We aim to identify an optimal motion plan with respect to robustness metric $R(\Pi, S)$, which can be expressed as an optimization problem:

$$\begin{aligned} \Pi^* &= \underset{\Pi}{\text{argmax}}\ R(\Pi, S) \\ \text{Subject to:}& \\ & C(\Pi) = 0 \\ & g_{\text{needle}}(\Pi) \geq 0 \\ & \mathbf{p}_1 \in S \\ & \mathbf{p}_n = \mathbf{p}_{\text{target}} \end{aligned}$$

where Π^* is an optimal plan, $C(\Pi) \mapsto [0, 1]$ is a collision detection function for which the result 0 corresponds to the plan being collision-free and the general inequality $g_{\text{needle}}(\Pi)$ represents the steerable needle's kinematic constraints.

IV. METHODS

In this section, we describe how to efficiently compute $R(\Pi, S)$ and a strategy to identify plans with a large valid insertion surface. To determine the valid insertion surface of a nominal motion plan Π, we construct a funnel along the plan that guarantees for each position inside the funnel that a collision-free motion plan to the target position $\mathbf{q}_{\text{target}}$ exists. A diagram of such a funnel is shown in Fig. 3. We first define the geometry of one funnel section around one plan section in subsection IV-A. Then, we introduce an algorithm to compute the funnel region of a full plan in subsection IV-B. In subsection IV-C, we describe how to project the funnel onto the insertion surface to determine the valid insertion surface and how to visualize this surface. Finally, in subsection IV-D, we describe how to modify an existing steerable needle motion planner to support planning from a region to a target postion.

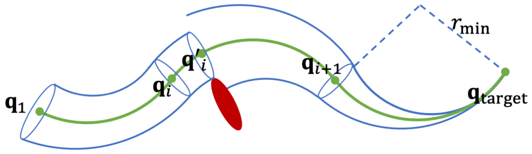

Fig. 3. We grow the funnel (blue) backward from $\mathbf{q}_{\text{target}}$ to $\mathbf{q}_1$ along the nominal steerable needle motion plan (green). The funnel is limited by the minimum radius of curvature $r_{\min}$. In the presence of obstacles (red), we shrink the diameter of the funnel to keep it collision-free, so the diameter of the funnel may be discontinuous with respect to distance along the nominal motion plan.

A. Funnel Section Geometry

In our method, each configuration along a nominal motion plan is associated with a funnel section. A funnel section can be defined as a three-tuple $\psi = (\mathbf{q}, d, \beta)$, where $\mathbf{q}$ is the configuration it is associated to, d is the distance from the center to the funnel boundary, and β is the difference in tangent direction between $\mathbf{q}$ and the funnel boundary. From a geometry perspective, the funnel of a motion plan is a sequence of circles that are centered along the nominal motion plan and lie in planes perpendicular to the plan.

The funnel sections can be defined recursively. More specifically, given a known funnel section $\psi_{i+1} = (\mathbf{q}_{i+1}, d_{i+1}, \beta_{i+1})$ and a section of the nominal motion plan ρ_i connecting $\mathbf{q}_i$ and $\mathbf{q}_{i+1}$, we can compute the funnel section $\psi_i = (\mathbf{q}_i, d_i, \beta_i)$ centered at $\mathbf{q}_i$.

The core idea of computing ψ_i is to extend the funnel boundary at ψ_{i+1} with maximum curvature curves, and when such curves reach the cross section at ψ_i, we take the minimum distance to $\mathbf{p}_i$ as d_i. The minimum distance is always obtained within the plane that the nominal motion plan section lies in. The detailed geometry is shown in Fig. 4. Recall that our goal is to compute ψ_i, and since $\mathbf{q}_i$ is known, we only need to determine d_i and β_i. Given that funnel section ψ_{i+1} and minimum radius of curvature $r_{\min}$ are known, we compute $\mathbf{c}'_i$, which is the center of the maximum curvature arc. Similarly, the nominal motion plan section (parameterized with $\mathbf{q}_{i+1}, r_i$, and α_i) is also given, and we can compute the center of the centered motion plan section $\mathbf{c}_i$. Then, we compute the chord length considering the line passing $\mathbf{c}_i$ and $\mathbf{p}_i$ and the circle centered at $\mathbf{c}'_i$ with radius $r_{\min}$. Additionally, with the distance between $\mathbf{c}_i$ and the projection of $\mathbf{c}'_i$ on line $(\mathbf{c}_i, \mathbf{p}_i)$, we subsequently get the length of line segment $(\mathbf{c}_i, \mathbf{f}_i)$, denoted as $\|\mathbf{c}_i - \mathbf{f}_i\|_2$. Given $\|\mathbf{c}_i - \mathbf{p}_i\|_2 = r_i$, we now have

$$d_i = r_i - \|\mathbf{c}_i - \mathbf{f}_i\|_2.$$

With $\mathbf{f}_{i+1}$ known and $\mathbf{f}_i$ computed as above, we can then compute α'_i. Finally, the difference in tangent direction can be computed as

$$\beta_i = \beta_{i+1} + \alpha'_i - \alpha_i.$$

It can be seen that from any point $\mathbf{g}_i$ inside the funnel section ψ_i, with any orientation bounded with the orientation of configuration $\mathbf{q}_i$ and the orientation at the funnel boundary, there exists a kinematically feasible curve that reaches a point $\mathbf{g}_{i+1}$ inside the funnel section ψ_{i+1}. The orientation at $\mathbf{g}_{i+1}$ is bounded with the orientation of $\mathbf{q}_{i+1}$ and the orientation at the boundary of funnel ψ_{i+1}.

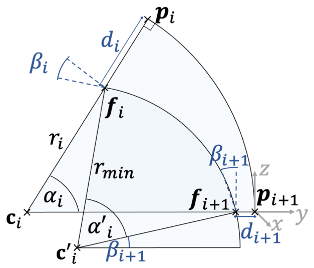

Fig. 4. The funnel along a plan section $(\mathbf{q}_{i+1}, \mathbf{q}_i)$ expands from a radius of d_{i+1} at $\mathbf{q}_{i+1}$ to a radius of d_i at $\mathbf{q}_i$ based on the steerable needle's minimum radius of curvature $r_{\min}$. The funnel's angular deviation from the deployment direction of the steerable needle grows from β_{i+1} to β_i.

This funnel definition is a conservative one, as we limit funnel growth to the target orientation of the nominal motion plan. Therefore, the funnel does not contain all steerable needle configurations for which plans to $\mathbf{p}_{\text{target}}$ exist. However, this strategy provides us with an estimate of a plan's start position robustness that is computationally lightweight and allows for a circular funnel representation.

B. Computing the Funnel

We define the funnel as an ordered list $\psi = [\psi_1, \ldots, \psi_n]$, where each funnel section ψ_i corresponds to a steerable needle plan configuration $\mathbf{q}_i$. We compute the funnel's expansion along a plan Π backwards against the steerable needle's deployment direction. This process is outlined in Alg. 1.

We begin at the plan's target configuration $\mathbf{q}_{\text{target}}$ and follow the plan towards its start configuration $\mathbf{q}_1$. The funnel section corresponding to $\mathbf{q}_{\text{target}}$ is $\psi_t = \{\mathbf{q}_t, 0, 0\}$, as the funnel converges toward the plan's target configuration (Alg. 1, line 2). Starting at the target, we iterate over each plan section ρ_i. We take steps of size s along each plan section of length l_i. For each step, we compute $\mathbf{q}_c$, the current configuration along the arc represented in ρ_i, by interpolating between $\mathbf{q}_{i+1}$ and $\mathbf{q}_i$ starting at $\mathbf{q}_{i+1}$ (Alg. 1, line 8). Then, we compute the funnel's expansion from ψ_{i+1} at configuration $\mathbf{q}_{i+1}$ to $\mathbf{q}_c$ as described in subsection IV-A, resulting in current funnel section ψ_c. Finally, we test ψ_c for collisions with obstacles (Alg. 1, line 10).

To ensure a collision-free funnel, we compute the minimum distance to the current configuration $\mathbf{q}_c$:

$$\text{FunnelCollisionDistance}(\mathbf{q}_c) = \underset{\mathbf{v} \in \mathcal{O}}{\text{argmin}}\ ||\mathbf{p}_c - \mathbf{v}||_2.$$

If the minimum distance to an obstacle for $\mathbf{q}_c$ is smaller than the current funnel radius d_c, the funnel is considered to be in collision. In this case, we reduce the funnel radius to $d'_c = \text{FunnelCollisionDistance}(\mathbf{q}_c)$. We also reduce the angular deviation β'_c to zero as our method does not provide guarantees for specific orientations. We assume that the steerable needle can be automatically rotated at its insertion point through an aiming device. We add $\psi'_c = \{\mathbf{q}_c, d'_c, \beta'_c\}$ to the front of ordered list ψ (Alg. 1, lines 12 - 14). For consistency, we modify the nominal motion plan by inserting

Algorithm 1 Funnel Computation

```
1:  function FUNNELCOMPUTATION($\Pi$, $\mathcal{O}$,$s$)
2:      $\psi[0] \leftarrow \{0,0\}$
3:      $\Pi' \leftarrow \Pi$
4:      for $i = n : -1 : 1$ do
5:          $l = l_i$
6:          for $j = l_i : -s : 0$ do
7:              $l_c = js$
8:              $\Pi_c \leftarrow$ Interpolate($\rho_i$, $l_c$)
9:              $\psi_c \leftarrow$ FunnelParameters($\psi[0]$, $\rho_c$, $l_c$)
10:             $d \leftarrow$ FunnelCollisionDistance($\mathbf{q}_c$)
11:             if not $d_c \leq d$ then
12:                 $d_c = d$
13:                 $\beta_c = 0$
14:                 $\psi$.pushFront($\psi_c$)
15:                 $l_i \leftarrow l_i - l_c$
16:                 $\Pi'$.Insert($\rho_c, i$)
17:         $\psi$.pushFront($\psi_c$)
        return $\Pi'$, $\psi$
```

an additional plan section ρ_c: $\Pi' = [\ldots, \rho_i, \rho_c, \rho_{i+1}, \ldots]$, with $\rho_c = \{\mathbf{q}_c, r_i, l_c, \gamma_i\}$. We set the remaining length of ρ_i to $l_i - l_c$ and we proceed to analyze the remaining plan section (Alg. 1, lines 15 - 16).

When we reach the end of the arc at $\mathbf{q}_i$, we add the latest funnel section ψ_c to list ψ (Alg. 1, line 17). After iterating over all plan segments as described above, the final size of the funnel is ψ_1 around $\mathbf{p}_1$. A diagram of a complete funnel is shown in Fig. 3.

C. Valid Insertion Surface

The final radius of the funnel at the nominal motion plan's start configuration provides a metric of how robust the steerable needle plan is to deviations. However, we also have to take into account which areas of the funnel are actually reachable from the insertion surface S. To do so, we project the funnel opening onto S to determine a valid insertion surface U, which is a subset of S. The valid insertion surface consists of suitable alternative start positions from which the target can be reached. We represent S by a triangular mesh T_S, a common representation used when modeling surfaces in 3D anatomical models. For each triangle in T_S, we determine if it represents valid insertion positions. Beginning at triangle t_1, which contains the target insertion point $\mathbf{p}_1$, we perform a breadth-first search among neighboring triangles. We evaluate each triangle based on the criteria outlined below. If a triangle t fulfills the criteria, we expand the search to its neighboring triangles and we add t to $T_U \subset T_S$, the set of valid insertion triangles.

We evaluate each triangle t as follows: first, we test if t lies within the funnel. We find the position $\mathbf{p}_i$ along the plan that is closest to $\mathbf{g}$, the centroid of t. We determine r_{triangle}, the radius of the smallest circle centered at $\mathbf{g}$ that envelops the entire triangle. The triangle is completely inside the funnel if

$$||\mathbf{g} - \mathbf{p}_i||_2 + r_{\text{triangle}} \leq d_i,$$

where d_i is the funnel radius at $\mathbf{p}_i$. For those triangles that are positioned beyond the funnel but could be within reach, we extend the steerable needle motion plan. This occurs because the surface of T_S is three-dimensional and therefore does not always perfectly coincide with the surface of the funnel. We add an additional straight section before the original start configuration and we compute a corresponding funnel section as described in section IV-A. We consider all triangles within this extension to represent valid insertion positions as well. Fig. 5a visualizes this procedure.

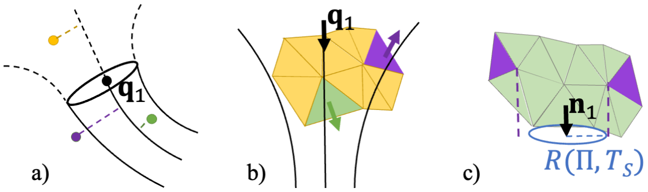

Fig. 5. a) To be part of the valid insertion surface U, triangles should be completely inside the funnel (green) or its extension (yellow). Triangles partially outside the funnel (purple) are not considered to be reachable. b) Only triangles (green) whose surface normal deviates less than 90 degrees from the plans initial deployment direction $\mathbf{q}_1$ are considered to be part of T_U, other triangles (purple) are not. c) We project triangle positions onto a plane normal to $\mathbf{n}_1$, the surface normal at the target insertion point. Robustness metric $R(\Pi, T_S)$ is the radius of the largest circle that does not contain triangles that are not part of T_U.

Next, we test if the triangle is oriented such that the funnel can be reached. We assume that the steerable needle can take on any orientation on the surface by using an aiming device [6]. Therefore, it can reach the funnel from triangle t if

$$\cos^{-1}\left(\frac{\mathbf{n}_t \cdot \mathbf{z}}{||\mathbf{z}|| \cdot ||\mathbf{n}_t||}\right) \leq \frac{\pi}{2},$$

where $\mathbf{n}_t$ is the surface normal of triangle t and $\mathbf{z}$ is the steerable needle's deployment direction in $\mathbf{q}_1$ (see Fig. 5b). This is a conservative limit as it does not take the steerable needle's ability to curve into consideration. If both criteria are met, we expand the search to the triangle's unseen neighbors in T_S and add t to T_U. After the search is terminated, we paint all triangles in the valid insertion surface according to their distance to the funnel boundary as shown in Fig. 1. This coloring scheme results in a bullseye representation centered around the target insertion point $\mathbf{p}_1$.

To quantify the size of the valid insertion surface U, we determine its radius according to Eq. 1. Therefore, we project the centroids $\mathbf{g}$ of all triangles in T_U onto the plane in which the circle lies:

$$\mathbf{g}' = \mathbf{g} - (\mathbf{n}_1 \cdot (\mathbf{p}_1 - \mathbf{g}))\ \mathbf{n}_1), \tag{2}$$

as shown in Fig. 5c. Now we determine the maximum radius such that all triangles closer to the target insertion point than this distance are part of the valid insertion surface:

$$\begin{aligned} R(\Pi, T_S) &= \max\ w \\ &\text{s. t. } ||\mathbf{g}'_j - \mathbf{p}_1||_2 - r_{\text{triangle}} > w\ \forall t_j \in T_S \setminus T_U, j \in \mathbb{N} \end{aligned}$$

where $\mathbf{g}'_j$ is the projection of the centroid of triangle t_j according to Eq. 2. This metric expresses how far from the target insertion point the initial steerable needle's insertion can deviate on the insertion surface such that a plan to the target still exists.

D. Backward Planning Strategy

To create nominal motion plans that we integrate with our new metric, we use a backward planning strategy. We previously showed that this strategy efficiently finds plans from a region to a point [19]. Although it is geared towards sampling based planners, this strategy can be used in combination with any steerable needle motion planner.

Our strategy involves planning backwards from the target toward T_S. With probability p, instead of extending an existing partial plan (e.g., by adding a new node to a tree structure), we sample a new orientation at $\mathbf{p}_{\text{target}}$ and start a new planning process form this new start pose. Thereby, we create multiple, potentially interleaving planning processes simultaneously until the planner finds a connection from T_S to the target position. To make this strategy more efficient, we prune nodes that cannot connect to T_S. When a sampling-based planner is used, an additional speedup can be achieved by biasing tree growth towards T_S.

We run the planner in an anytime manner, i.e., we repeat the planning process as time permits. Over time, the planner finds new plans and keeps a record of the plan with highest robustness that allow for more deviation in the needle's start configuration. The algorithm returns the best nominal motion plan Π according to R, the desired insertion point $\mathbf{p}_1$, and the valid insertion surface specified by T_U from which a motion plan to $\mathbf{p}_{\text{target}}$ is guaranteed to exist. For each new needle plan found, we compute its robustness measure $R(\Pi, T_S)$.

V. EVALUATION

We tested our approach in a lung biopsy scenario. Lung cancer is responsible for the most cancer-related deaths in the United States [41]. Early diagnosis through biopsy can increase a patient's chances of survival. A novel approach for safe lung nodule biopsy involves a physician navigating a bronchoscope through the airways and piercing a steerable needle through the airway wall into the lung parenchyma, and then handing off control of the procedure to a robot that autonomously steers the needle to the target [42], [4]. Using a steerable needle in a biopsy procedure can potentially mitigate patient risk, as the needle is able to avoid collisions with critical obstacles.

To model this scenario, we used a CT scan of in-vivo human lungs from the Lung Image Database Consortium and Image Database Resource Initiative (LIDC-IDRI) image collection [43] with a voxel size of $(0.6 \times 0.6 \times 0.7)$mm. We segmented the anatomy relevant for the obstacle map using the method described in [44]. We used the surface of the segmented airways as the insertion surface for the steerable needle. We represented the surface by a triangular mesh that we created with 3D Slicer [45]. We classified major blood vessels and the boundary of the lung parenchyma as obstacles. For collision detection, we use a nearest neighbor search structure [46] containing the positions of all voxels classified as obstacles in $\mathcal{O}$ as it allows for efficient detection of voxels inside the funnel structure. We then randomly sampled 50 target positions in the lung with a minimum distance of 1mm to obstacles. The lung environment as well as the targets are shown in Fig. 6.

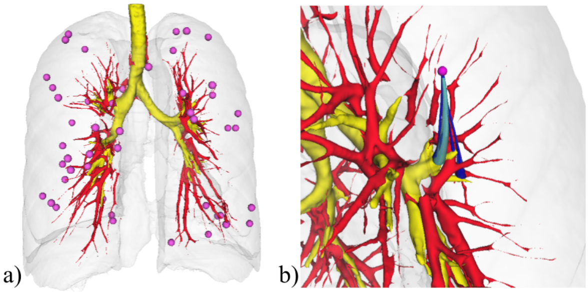

Fig. 6. a) The planning environment consists of the area inside the lung parenchyma (grey). Major blood vessels (red) are considered critical obstacles that have to be avoided. For each target (pink), we attempt to find plans from the airways (yellow). b) For each plan found, we construct a funnel around it (dark blue) to determine its start position robustness. We choose the most robust plan with the largest valid insertion surface (light blue).

We used the following steerable needle hardware parameters in this simulation: the steerable needle's diameter was $d_{\text{needle}} = 1.0$mm, the maximum insertion length was $l_{\text{needle}} = 150$mm, and the minimum radius of curvature was $r_{\text{min}} = 100$mm, which is a conservative measure suitable for medical applications [4], [1]. All simulations were run on a 3.7GHz 20-thread Intel Core i9-10900K CPU with 16GB of RAM.

We demonstrated the versatility of our robustness metric by integrating our funnel evaluation with two different steerable needle planning algorithms. The first one is the steerable needle planner by Patil et al. [12], and the second one is an Asymptotic Optimality RRT (AO-RRT) [8] adapted to steerable needles. We ran both planners using a backward planning strategy described in subsection IV-D to find nominal motion plans. For speedup, both algorithms used goal sampling (with random samples from the insertion surface) and pruned new samples from which the surface could not be reached.

We also compared our funnel evaluation with a baseline sampling based robustness evaluation strategy. For this sampling based evaluation, we ran the steerable needle motion planner the same way as for our funnel evaluation, planning from a goal position towards the insertion surface. For each new plan found after t_i seconds, we determined all triangles closer to the start configuration than the start configuration's minimum distance to an obstacle. We then re-ran the steerable needle planner, this time not terminating after one connection to the surface is found, but extending the search tree with the goal of reaching all of these triangles. To make a fair comparison, we included goal biasing with a probability of 0.1 per sample, as was done in [19]. We also pruned samples from which none of the triangles could be reached. We terminated the tree extension process when either plans to all eligible triangles were found or if no new plan to a previously not reached triangle was found in the past $2t_i$ seconds. Then, we determined the minimum distance to the closest triangle to which no plan from the goal was found.

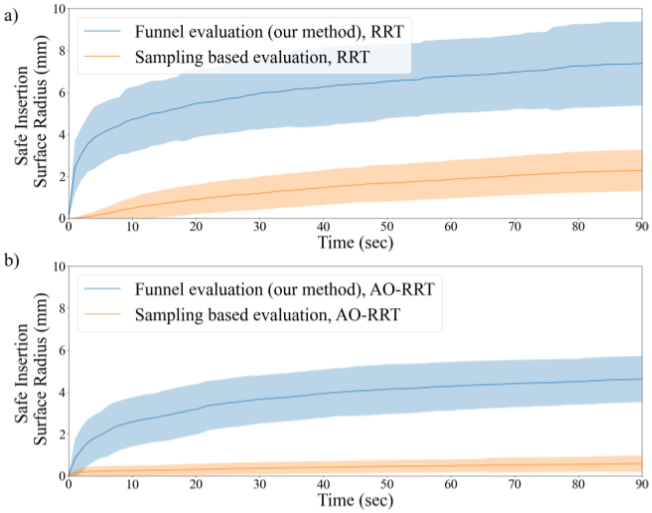

Fig. 7. We recorded plans the largest valid insertion surface found over time for each target and computed the average and standard deviation across 10 runs. Our funnel evaluation strategy finds plans with larger valid surfaces faster than the sampling based evaluation strategy, both in combination with a) the Steerable Needle RRT and b) the AO-RRT algorithm.

Our planning experiment consisted of running the planning process 10 times for a duration of 90 seconds to each target. During each planning process, we tracked the largest valid insertion surface found over time. We perform this process for four algorithms: (i) sampling-evaluated steerable needle RRT (ii) funnel-evaluated steerable needle RRT (iii) sampling-evaluated AO-RRT and (iv) funnel-evaluated AO-RRT. As the sampling based evaluation depends on the used motion planning algorithm, we implemented both a steerable needle RRT and AO-RRT version.

Fig. 7 visualizes the simulation results for all four combinations of planning algorithms and evaluation strategies. For each of the 50 targets the respective planner ran for 90 seconds. We evaluated each plan found according to the size of its valid insertion surface, saving the best plan found for each target over time. We repeated this process 10 times and determined the mean and standard deviation of the largest valid insertion surface found across runs for each target over time. The funnel evaluation in combination with the Steerable Needle RRT algorithm is able to find a plan with a valid insertion surface with an average radius of 7.4 mm (2.0 mm standard deviation per target). When applied to plans found by the AO-RRT algorithm, it finds plans with an average radius of 4.6 (1.1 mm standard deviation). The sampling-based evaluation strategy only finds an average radius of 2.3 mm (1.0mm standard deviation) with the Steerable Needle RRT and 0.6 mm (0.4 mm standard deviation) with the AO-RRT. The Steerable Needle RRT finds more plans in the same amount of time than the AO-RRT and therefore finds plans with larger valid insertion surfaces faster.

VI. CONCLUSION

In this work, we introduce a metric to evaluate steerable needle motion plans that considers uncertainty in the planned start position due to inherent imprecision in preceding deployment stages. We then introduce a strategy to evaluate this metric that is agnostic to the motion planner used to derive the nominal plans. To this end, we construct a funnel around the steerable needle motion plan based on the steerable needle's non-holonomic constraints and surrounding obstacles. We project the funnel onto the insertion surface to determine valid insertion positions. We express the size of this valid insertion surface through a robustness measure and we describe a planning scheme that finds steerable needle plans optimal with respect to this measure. In simulation, we show that our method finds plans with larger valid insertion surfaces faster than a sampling based method. This result is consistent across different motion planning algorithms in our study, always finding valid insertion surfaces at least more than 3 times larger than the sampling based method. More importantly, our strategy provides a guarantee that for any position on the valid insertion surface a plan to the target exists. We also provide a tool to visualize that surface, providing guidance to physicians.

While our method provides guidance to the needle insertion position, it assumes an aiming device to adjust the initial orientation. However, in some scenarios the aiming device may be limited to restricted orientations, which should be considered by the robustness metric. We are planning to extend the metric computation accordingly. We are hoping to test our funnel evaluation strategy and its bullseye visualization in procedures in animal tissues.

REFERENCES

[1] P. J. Swaney, A. W. Mahoney, B. I. Hartley, A. A. Remirez, E. Lamers, R. H. Feins, R. Alterovitz, and R. J. Webster III, "Toward transoral peripheral lung access: Combining continuum robots and steerable needles," *Journal of Medical Robotics Research*, vol. 2, no. 01, p. 1750001, 2017.

[2] M. Pinzi, S. Galvan, and F. Rodriguez y Baena, "The adaptive hermite fractal tree (AHFT): a novel surgical 3d path planning approach with curvature and heading constraints," *International Journal of Computer Assisted Radiology and Surgery*, vol. 14, no. 4, pp. 659–670, 2019.

[3] N. J. van de Berg, F. C. Meeuwsen, M. Doukas, G. Kronreif, A. Moelker, and J. J. van den Dobbelsteen, "Steerable needles for radio-frequency ablation in cirrhotic livers," *Scientific Reports*, vol. 11, no. 1, pp. 1–9, 2021.

[4] M. Rox, M. Emerson, T. E. Ertop, I. Fried, M. Fu, J. Hoelscher, A. Kuntz, J. Granna, J. Mitchell, M. Lester, F. Maldonado, E. A. Gillaspie, J. A. Akulian, R. Alterovitz, and R. J. Webster, "Decoupling steerability from diameter: Helical dovetail laser patterning for steerable needles," *IEEE Access*, vol. 8, pp. 181 411–181 419, 2020.

[5] A. Majewicz and A. M. Okamura, "Cartesian and joint space teleoperation for nonholonomic steerable needles," in *2013 World Haptics Conference (WHC)*. IEEE, 2013, pp. 395–400.

[6] M. Rox, M. Emerson, T. E. Ertop, M. Fu, I. Fried, J. Hoelscher, A. Kuntz, J. Granna, J. Mitchell, M. Lester, F. Maldonado, E. Gillaspie, J. Akulian, R. Alterovitz, and R. J. Webster III, "An aiming device for steerable needles," in *IEEE/ASME International Conference on Advanced Intelligent Mechatronics*. IEEE, 2020.

[7] S. Patil, J. Burgner, R. J. Webster, and R. Alterovitz, "Needle steering in 3-d via rapid replanning," *IEEE Transactions on Robotics*, vol. 30, no. 4, pp. 853–864, 2014.

[8] K. Hauser and Y. Zhou, "Asymptotically optimal planning by feasible kinodynamic planning in a state–cost space," *IEEE Transactions on Robotics*, vol. 32, no. 6, pp. 1431–1443, 2016.

[9] N. J. Cowan, K. Goldberg, G. S. Chirikjian, G. Fichtinger, R. Alterovitz, K. B. Reed, V. Kallem, W. Park, S. Misra, and A. M. Okamura, "Robotic needle steering: Design, modeling, planning, and image guidance," in *Surgical Robotics*. Springer, 2011, pp. 557–582.

[10] M. Fu, O. Salzman, and R. Alterovitz, "Toward certifiable motion planning for medical steerable needles," in *Proc. Robotics Science and Systems (RSS)*. RSS, 2021, pp. 1–16.

[11] V. Duindam, J. Xu, R. Alterovitz, S. Sastry, and K. Goldberg, "Three-dimensional motion planning algorithms for steerable needles using inverse kinematics," *The International Journal of Robotics Research*, vol. 29, no. 7, pp. 789–800, 2010.

[12] S. Patil and R. Alterovitz, "Interactive motion planning for steerable needles in 3d environments with obstacles," in *Proc. IEEE RAS & EMBS International Conference on Biomedical Robotics and Biomechatronics*, 2010, pp. 893–899.

[13] S. M. LaValle, "Rapidly-exploring random trees: A new tool for path planning," *TR 98-11, Computer Science Dept., Iowa State Univ.*, 1998.

[14] D. Berenson, S. S. Srinivasa, D. Ferguson, A. Collet, and J. J. Kuffner, "Manipulation planning with workspace goal regions," in *Proc. International Conference on Robotics and Automation (ICRA)*. IEEE, 2009, pp. 618–624.

[15] S. Karaman, M. R. Walter, A. Perez, E. Frazzoli, and S. Teller, "Anytime motion planning using the RRT," in *Proc. International Conference on Robotics and Automation (ICRA)*. IEEE, 2011, pp. 1478–1483.

[16] K. Yang, "An efficient spline-based RRT path planner for non-holonomic robots in cluttered environments," in *2013 International Conference on Unmanned Aircraft Systems (ICUAS)*. IEEE, 2013, pp. 288–297.

[17] R. Alterovitz, K. Goldberg, and A. Okamura, "Planning for steerable bevel-tip needle insertion through 2d soft tissue with obstacles," in *Proc. International Conference on Robotics and Automation (ICRA)*. IEEE, 2005, pp. 1640–1645.

[18] A. Kuntz, L. G. Torres, R. H. Feins, R. J. Webster, and R. Alterovitz, "Motion planning for a three-stage multilumen transoral lung access system," in *Proc. IEEE/RSJ International Conference on Intelligent Robots and Systems (IROS)*, 2015, pp. 3255–3261.

[19] J. Hoelscher, M. Fu, I. Fried, M. Emerson, T. E. Ertop, M. Rox, A. Kuntz, J. A. Akulian, R. J. Webster III, and R. Alterovitz, "Backward planning for a multi-stage steerable needle lung robot," *Robotics and Automation Letters (RA-L)*, vol. 6, no. 2, pp. 3987–3994, 2021.

[20] J. W. Cannon, J. A. Stoll, S. D. Selha, P. E. Dupont, R. D. Howe, and D. F. Torchiana, "Port placement planning in robot-assisted coronary artery bypass," *Transactions on Robotics and Automation*, vol. 19, no. 5, pp. 912–917, 2003.

[21] L. Adhami and É. Coste-Maniére, "A versatile system for computer integrated mini-invasive robotic surgery," in *International Conference on Medical Image Computing and Computer-Assisted Intervention*. Springer, 2002, pp. 272–281.

[22] M. Feng, X. Jin, W. Tong, X. Guo, J. Zhao, and Y. Fu, "Pose optimization and port placement for robot-assisted minimally invasive surgery in cholecystectomy," *The International Journal of Medical Robotics and Computer Assisted Surgery*, vol. 13, no. 4, p. e1810, 2017.

[23] Y. Hayashi, K. Misawa, and K. Mori, "Optimal port placement planning method for laparoscopic gastrectomy," *International Journal of Computer Assisted Radiology and Surgery*, vol. 12, no. 10, pp. 1677–1684, 2017.

[24] L. W. Sun and C. K. Yeung, "Port placement and pose selection of the da Vinci surgical system for collision-free intervention based on performance optimization," in *Proc. International Conference on Intelligent Robots and Systems (IROS)*. IEEE, 2007, pp. 1951–1956.

[25] S. Niyaz, A. Kuntz, O. Salzman, R. Alterovitz, and S. S. Srinivasa, "Optimizing motion-planning problem setup via bounded evaluation with application to following surgical trajectories," in *Proc. IEEE/RSJ International Conference on Intelligent Robots and Systems (IROS)*. IEEE, 2019, pp. 1355–1362.

[26] J. Motes, R. Sandström, W. Adams, T. Ogunyale, S. Thomas, and N. M. Amato, "Interaction templates for multi-robot systems," *IEEE Robotics and Automation Letters (RA-L)*, vol. 4, no. 3, pp. 2926–2933, 2019.

[27] R. Shome and K. E. Bekris, "Anytime multi-arm task and motion planning for pick-and-place of individual objects via handoffs," in *2019 International Symposium on Multi-Robot and Multi-Agent Systems (MRS)*. IEEE, 2019, pp. 37–43.

[28] N. Vahrenkamp, D. Berenson, T. Asfour, J. Kuffner, and R. Dillmann, "Humanoid motion planning for dual-arm manipulation and re-grasping tasks," in *2009 IEEE/RSJ International Conference on Intelligent Robots and Systems*. IEEE, 2009, pp. 2464–2470.

[29] I. D. Walker, L. Mears, R. S. Mizanoor, R. Pak, S. Remy, and Y. Wang, "Robot-human handovers based on trust," in *2015 Second International Conference on Mathematics and Computers in Sciences and in Industry (MCSI)*. IEEE, 2015, pp. 119–124.

[30] J. Mainprice, M. Gharbi, T. Siméon, and R. Alami, "Sharing effort in planning human-robot handover tasks," in *Proc. International Symposium on Robot and Human Interactive Communication (RO-MAN)*. IEEE, 2012, pp. 764–770.

[31] N. Vahrenkamp, H. Arnst, M. Wächter, D. Schiebener, P. Sotiropoulos, M. Kowalik, and T. Asfour, "Workspace analysis for planning human-robot interaction tasks," in *Proc. International Conference on Humanoid Robots (Humanoids)*. IEEE, 2016, pp. 1298–1303.

[32] W. Park, J. S. Kim, Y. Zhou, N. J. Cowan, A. M. Okamura, and G. S. Chirikjian, "Diffusion-based motion planning for a nonholonomic flexible needle model," in *Proc. International Conference on Robotics and Automation (ICRA)*. IEEE, 2005, pp. 4600–4605.

[33] R. Alterovitz, M. Branicky, and K. Goldberg, "Motion planning under uncertainty for image-guided medical needle steering," *The International Journal of Robotics Research*, vol. 27, no. 11-12, pp. 1361–1374, 2008.

[34] W. Sun, S. Patil, and R. Alterovitz, "High-frequency replanning under uncertainty using parallel sampling-based motion planning," *IEEE Transactions on Robotics*, vol. 31, no. 1, pp. 104–116, 2015.

[35] W. Sun, J. Van Den Berg, and R. Alterovitz, "Stochastic extended LQR: Optimization-based motion planning under uncertainty," in *Algorithmic Foundations of Robotics XI*. Springer, 2015, pp. 609–626.

[36] A. Favaro, L. Cerri, S. Galvan, F. Rodriguez y Baena, and E. De Momi, "Automatic optimized 3d path planner for steerable catheters with heuristic search and uncertainty tolerance," in *Proc. International Conference on Robotics and Automation (ICRA)*. IEEE, 2018, pp. 9–16.

[37] R. Tedrake, "LQR-trees: Feedback motion planning on sparse randomized trees," in *Proc. Robotics Science and Systems (RSS)*. RSS, 2009.

[38] R. J. Webster III, J. S. Kim, N. J. Cowan, G. S. Chirikjian, and A. M. Okamura, "Nonholonomic modeling of needle steering," *The International Journal of Robotics Research*, vol. 25, no. 5-6, pp. 509–525, 2006.

[39] D. S. Minhas, J. A. Engh, M. M. Fenske, and C. N. Riviere, "Modeling of needle steering via duty-cycled spinning," in *2007 29th Annual International Conference of the IEEE Engineering in Medicine and Biology Society*. IEEE, 2007, pp. 2756–2759.

[40] H. Choset and W. Henning, "A follow-the-leader approach to serpentine robot motion planning," *Journal of Aerospace Engineering*, vol. 12, no. 2, pp. 65–73, 1999.

[41] American Cancer Society, "Cancer facts and figures," *American Cancer Society Tech. Rep.*, 2018.

[42] A. Kuntz, P. J. Swaney, A. Mahoney, R. H. Feins, Y. Z. Lee, R. J. Webster III, and R. Alterovitz, "Toward transoral peripheral lung access: Steering bronchoscope-deployed needles through porcine lung tissue," in *Hamlyn Symposium on Medical Robotics*, 2016, pp. 9–10.

[43] S. G. Armato III, G. McLennan, L. Bidaut, M. F. McNitt-Gray, C. R. Meyer, A. P. Reeves, B. Zhao, D. R. Aberle, C. I. Henschke, E. A. Hoffman, *et al.*, "The lung image database consortium (LIDC) and image database resource initiative (IDRI): a completed reference database of lung nodules on ct scans," *Medical physics*, vol. 38, no. 2, pp. 915–931, 2011.

[44] M. Fu, A. Kuntz, R. J. Webster, and R. Alterovitz, "Safe motion planning for steerable needles using cost maps automatically extracted from pulmonary images," in *Proc. IEEE/RSJ International Conference on Intelligent Robots and Systems (IROS)*. IEEE, 2018, pp. 4942–4949.

[45] R. Kikinis, S. D. Pieper, and K. G. Vosburgh, "3d slicer: a platform for subject-specific image analysis, visualization, and clinical support," in *Intraoperative imaging and image-guided therapy*. Springer, 2014, pp. 277–289.

[46] J. Ichnowski and R. Alterovitz, "Concurrent nearest-neighbor searching for parallel sampling-based motion planning in SO(3), SE(3), and euclidean spaces," *Springer*, 2018.